

REPORT DOCUMENTATION PAGE				Form Approved OMB No. 0704-0188	
Public reporting burden for this collection of information is estimated to average 1 hour per response, including the time for reviewing instructions, searching existing data sources, gathering and maintaining the data needed, and completing and reviewing this collection of information. Send comments regarding this burden estimate or any other aspect of this collection of information, including suggestions for reducing this burden to Department of Defense, Washington Headquarters Services, Directorate for Information Operations and Reports (0704-0188), 1215 Jefferson Davis Highway, Suite 1204, Arlington, VA 22202-4302. Respondents should be aware that notwithstanding any other provision of law, no person shall be subject to any penalty for failing to comply with a collection of information if it does not display a currently valid OMB control number. PLEASE DO NOT RETURN YOUR FORM TO THE ABOVE ADDRESS.					
1. REPORT DATE (DD-MM-YYYY) 15-05-2006		2. REPORT TYPE Technical Paper		3. DATES COVERED (From - To)	
4. TITLE AND SUBTITLE Evolution of the Ion Velocity Distribution in the Near Field of the BHT-200-X3 Hall Thruster (Postprint)				5a. CONTRACT NUMBER	
				5b. GRANT NUMBER	
				5c. PROGRAM ELEMENT NUMBER	
6. AUTHOR(S) William A. Hargus, Jr. (AFRL/PRSS); Michael R. Nakles (ERC)				5d. PROJECT NUMBER 23080535	
				5e. TASK NUMBER	
				5f. WORK UNIT NUMBER	
7. PERFORMING ORGANIZATION NAME(S) AND ADDRESS(ES) Air Force Research Laboratory (AFMC) AFRL/PRSS 1 Ara Drive Edwards AFB CA 93524-7013				8. PERFORMING ORGANIZATION REPORT NUMBER AFRL-PR-ED-TP-2006-128	
9. SPONSORING / MONITORING AGENCY NAME(S) AND ADDRESS(ES) Air Force Research Laboratory (AFMC) AFRL/PRS 5 Pollux Drive Edwards AFB CA 93524-70448				10. SPONSOR/MONITOR'S ACRONYM(S)	
				11. SPONSOR/MONITOR'S NUMBER(S) AFRL-PR-ED-TP-2006-128	
12. DISTRIBUTION / AVAILABILITY STATEMENT Approved for public release; distribution unlimited (AFRL-ERS-PAS-2006-104).					
13. SUPPLEMENTARY NOTES © 2006 American Institute of Aeronautics and Astronautics, Inc. Presented at the 42 nd AIAA/ASME/SAE/ASEE Joint Propulsion Conference, Sacramento, CA, 9-12 July 2006. AIAA 2006-4991.					
14. ABSTRACT <p>This work presents an analysis of near plume velocity distributions of the Busek BHT-200-X3 200 W laboratory Hall thruster derived from laser-induced fluorescence measurements of the 5d[4]7/2-6p[3]5/2 xenon ion excited state transition. The evolution of the axial and radial velocity distributions is presented from the exit plane to approximately 0.7 exit diameters downstream. It is shown that the distributions evolve significantly between the exit channel center and the inner portion of the channel where there are high frac-tions of low velocity ions. It is believed that this may be due to the slight inward focus of the xenon ion propellant colliding on the surface, recombining, and subsequently being re-ionized. Low axial velocity ions appear downstream of the thruster exit plane. While their origin is not entirely certain, the most likely explanation appears to be cross annular flow. Strong evidence of charge exchange is also evident producing high velocity wings on the primary ion velocity peak reminiscent of ion energy analyzer studies of other thrusters. A survey of the axial and radial velocity distributions along the exposed exterior boron nitride nose cone covering the central magnetic pole is performed to determine the behavior of the ions impacting this critical surface. The VDF is ideal for comparison with numerical simulations since it allows for direct comparison of the fundamental ion acceleration. External VDF data can even provide limited insight as to the internal ion formation and acceleration processes.</p>					
15. SUBJECT TERMS					
16. SECURITY CLASSIFICATION OF:			17. LIMITATION OF ABSTRACT A	18. NUMBER OF PAGES 12	19a. NAME OF RESPONSIBLE PERSON Dr. William A. Hargus, Jr.
a. REPORT Unclassified	b. ABSTRACT Unclassified	c. THIS PAGE Unclassified			19b. TELEPHONE NUMBER (include area code) N/A

AIAA-2006-4991

Evolution of the Ion Velocity Distribution in the Near Field of the BHT-200-X3 Hall Thruster

William A. Hargus, Jr. *
Air Force Research Laboratory
Edwards AFB, CA 93524

Michael R. Nakles †
E.R.C. Inc.
Edwards AFB, CA 93524

Abstract

This work presents an analysis of near plume velocity distributions of the Busek BHT-200-X3 200 W laboratory Hall thruster derived from laser-induced fluorescence measurements of the $5d[4]_{7/2}-6p[3]_{5/2}$ xenon ion excited state transition. The evolution of the axial and radial velocity distributions is presented from the exit plane to approximately 0.7 exit diameters downstream. It is shown that the distributions evolve significantly between the exit channel center and the inner portion of the channel where there are high fractions of low velocity ions. It is believed that this may be due to the slight inward focus of the xenon ion propellant colliding on the surface, recombining, and subsequently being re-ionized. Low axial velocity ions appear downstream of the thruster exit plane. While their origin is not entirely certain, the most likely explanation appears to be cross annular flow. Strong evidence of charge exchange is also evident producing high velocity wings on the primary ion velocity peak reminiscent of ion energy analyzer studies of other thrusters. A survey of the axial and radial velocity distributions along the exposed exterior boron nitride nose cone covering the central magnetic pole is performed to determine the behavior of the ions impacting this critical surface. The VDF is ideal for comparison with numerical simulations since it allows for direct comparison of the fundamental ion acceleration. External VDF data can even provide limited insight as to the internal ion formation and acceleration processes.

Introduction

The goal of this study is to characterize the xenon ion velocity distribution function (VDF) of 200 W Busek BHT-200-X3 xenon Hall thruster in the region between the exit and cathode planes. The VDF is ideal for comparison with numerical simulations since it allows for direct comparison of the fundamental ion acceleration. External VDF data can even provide limited insight as to the internal ion formation and acceleration processes.

Many previous attempts to compare bulk ion velocities from experiments with results of numerical simulations have encountered difficulties. For example, simulation efforts usually report mean velocities. Experimental methods such as laser-induced fluorescence (LIF) are often noise limited and are better suited to determining the most probable velocity. In the skewed, non-symmetric velocity distributions common to Hall thrusters, the most probable (e.g. peak signal) and statistical mean velocities differ. Depending on the shape of the distribution, these two bulk measures of velocity may vary significantly. The advantage of using a single bulk velocity measure is that it allows for the succinct presentation of large data sets.

However, both the modeler and experimentalist are discarding the majority of the generated data. Comparison of the VDF determined from each method will allow for minimal ambiguity. Furthermore, the annular geometry of the Hall thruster discharge / acceleration chamber produces a complex flow field where multiple velocity populations interact. The comparison of VDF data in these cases is vital to increasing understanding of these flows.

Xenon Laser Induced Fluorescence

LIF is a convenient diagnostic for the investigation of the VDF as it does not perturb the plasma. The LIF signal is a convolution of the VDF, transition line shape, and laser beam frequency profile. Determination of the VDF from LIF data only requires the deconvolution the transition line shape and laser beam profile from the raw LIF signal.

For the results reported here, the $5d[4]_{7/2}-6p[3]_{5/2}$ electronic transition of Xe II at 834.7 nm is probed. The isotopic and nuclear-spin effects contributing to the hyperfine structure of the $5d[4]_{7/2}-6p[3]_{5/2}$ xenon ion transition produce a total of 19 isotopic and spin split components. The hyperfine splitting constants which characterize the variations in state energies are only known for a limited set of energy levels. Unfortunately, the 834.7 nm xenon ion transition only has confirmed data on

* Research Engineer, Senior Member AIAA

† Research Engineer, Member AIAA

the nuclear spin splitting constants of the $6p[3]_{5/2}$ upper state [1-4]. Manzella and others have previously used the $5d[4]_{7/2}$ - $6p[3]_{5/2}$ xenon ion transition at 834.7 nm to make velocity measurements in a Hall thruster plume [1,5-7]. A convenient feature of this transition is the presence of a relatively strong line originating from the same upper state ($6s[2]_{3/2}$ - $6p[3]_{5/2}$ transition at 541.9 nm [8] which allows for non-resonant fluorescence collection.

Ion velocity is determined by measurement of the Doppler shift of the absorbing ions. If an absorber has a velocity component u along the axis of the laser beam, it will absorb the light at a frequency shifted from that of stationary absorbers. The magnitude of this frequency shift $\partial\nu_{12}$ depends on the speed u along the laser beam axis

$$\partial\nu_{12} = \nu_{12} \frac{u}{c} \quad [1]$$

where c is the speed of light. The Doppler shift of a species' fluorescence profile away from the line center ν_{12} of stationary absorbers is in proportion to u [9].

Experimental Apparatus

The measurements in this effort were performed in Chamber 6 of the Air Force Research Laboratory (AFRL) Electric Propulsion Laboratory at Edwards AFB, CA. Chamber 6 is a non-magnetic stainless steel chamber with a 1.8 m diameter and 3 m length. It has a measured pumping speed of 32,000 l/s on xenon. Pumping is provided by four single stage cryogenic panels (single stage cold heads at ~ 25 K) and one 50 cm two stage cryogenic pump (< 12 K). Chamber pressure during thruster operation is approximately 7×10^{-4} Pa, corrected for xenon.

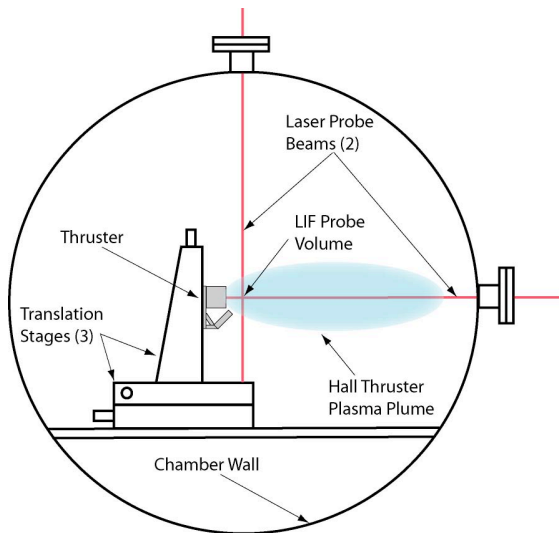


Fig. 1. Side view diagram of thruster within AFRL Chamber 6. Also shown are the translation stages and the laser probe beams. Note that the fluorescence collection and external optics are not shown.

The Hall thruster used in this study is the Busek Company BHT-200-X3 200 W Hall thruster which has been described elsewhere [10]. Table 1 shows the nominal operating conditions for the BHT-200-X3 thruster during this test. During thruster operation, the parameters shown in Table 1 are monitored and recorded at a 1 Hz data rate.

Table 1. Nominal Thruster Operating Conditions

Anode Flow	840 $\mu\text{g/s}$ (Xe)
Cathode Flow	98 $\mu\text{g/s}$ (Xe)
Anode Potential	250 V
Anode Current	0.82 A
Keeper Current	0.5 A
Magnet Current	1.0 A
Heater Current	3.0 A

Figure 1 shows a side-view diagram of the Hall thruster mounted within the vacuum chamber. The thruster is mounted on a three axes orthogonal computer controlled translation system. Figure 1 also shows the two orthogonal LIF probe beams and windows through which the beams enter the chamber. Figure 2 shows a top view of the laser optical train, collection optics, through which the beams end one leg of the external probe optics.

The laser used is a New Focus Vortex tunable diode laser. It is capable of tuning approximately ± 50 GHz about a center wavelength of 834.7 nm. The 10 mW beam is passed through a Faraday isolator to eliminate feedback to the laser. The laser beam then passes through several beam pick-offs until it reaches a 50-50 beam splitter (BS) where it is split into two beams of equal power. The first beam, the axial probe beam shown in Figs. 1 and 2, is focused by a lens and enters the vacuum chamber through a window. A second probe beam, shown in Fig. 1 only, is directed from the optical bench via a periscope apparatus so that it enters the chamber from above the thruster and probes the velocity perpendicular to the first probe beam. Each probe beam is chopped at a unique frequency by choppers Ch2 (2.8 kHz) and Ch3 (2.0 kHz) for simultaneous phase sensitive detection of the two fluorescence signals.

The two wedge beam pick-offs (/BS) shown in Fig. 2 provide portions of the beam for diagnostic purposes. The first beam pick-off directs a beam to a photodiode detector (D1) used to provide constant power feedback to the laser. The second beam is divided into two equal components by a 50-50 cube beam splitter. The first component is directed to an Burleigh WA-1500 wavemeter used to monitor absolute wavelength. The second component is sent through a chopper Ch1 (1.3 kHz) and through a low pressure xenon hollow cathode discharge lamp. The lamp provides a stationary absorption reference for the determination of the Doppler shift $\partial\nu_{12}$. Unfortunately, there is no detectable population of the ionic xenon

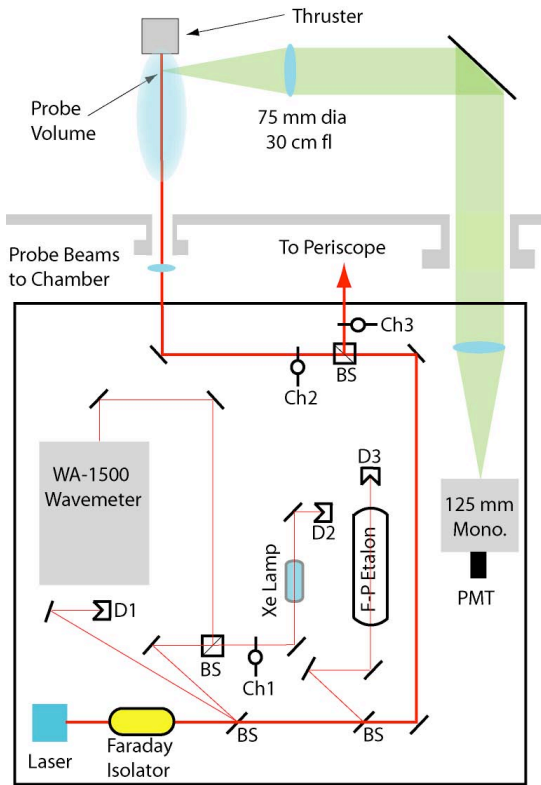


Fig. 2. Top view diagram of the laser optical train and collection optics. Note that the radial probe beam periscope and focusing optics are not shown.

$5d[4]_{7/2}$ state. However, there is a nearby (measured to be 17.6 GHz distant using this apparatus) neutral xenon $6s'[1/2]_1-6p'[3/2]_2$ transition at 834.68 nm [11-12]. The second pick-off sends a beam to a 300 MHz free spectral range Fabry-Perot etalon (F-P) that provides high resolution frequency monitoring of the wavelength interval swept during a laser scan.

The fluorescence collection optics are also shown in Fig. 2. The fluorescence is collected by a 75 mm diameter, 300 mm focal length lens within the chamber. The collimated fluorescence signal is directed through a window in the chamber side wall to a similar lens that focuses the collected fluorescence onto the entrance slit of 125 mm focal length monochromator with a photomultiplier tube (PMT). Due to the 1:1 magnification of the collection optics, the spatial resolution of the measurements is determined by the geometry of the entrance slit 1 mm width and 1.5 mm height as well as the sub-mm diameter of the probe beams.

Figure 3 shows the near field geometry of the Busek BHT-200 Hall thruster. The locations of the protruding central magnetic pole (nose cone) and edges of the acceleration channel are indicated as is the position of the cathode exit. The cartesian coordinate system and origin used in these measurements are also shown in Fig. 3. The coordinate system orientation is also referenced in Figs. 1 and 2. The origin is 0.5 mm beyond the tip of the nose cone due to the repeatability with which this position may be located. All locations are referenced to these coordinates. Measurements presented in this work will be limited to the Y-Z plane. Therefore in the anode discharge exit region, the Y axis velocity measurements correspond to the radial veloci-

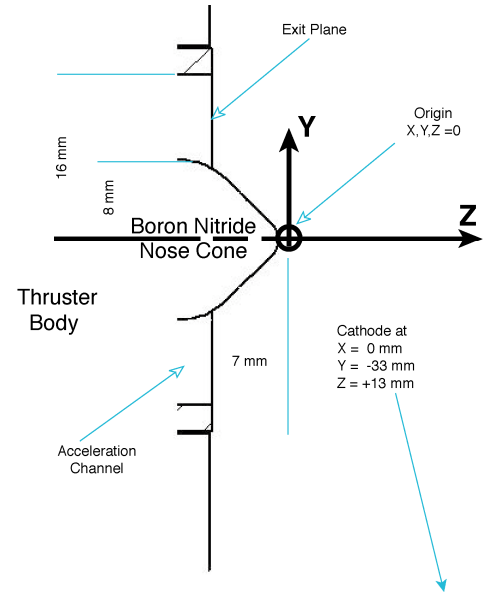


Fig. 3. Near field dimensions of the BHT-200-X3 Busek Co. Hall thruster with origin of the coordinate system and positions of critical dimensions and locations noted.

ties, and the Z axis measurements to the axial velocities.

Velocity Distribution Extraction

The convolution of two functions $a(t)$ and $z(t)$ is defined as

$$\int a(\tau)z(t-\tau)d\tau = a(t) * z(t) = u(t) \quad [2]$$

where $*$ denotes convolution and $u(t)$ is the resulting convolved function. In the specific case of interest here, $u(t)$ is the raw LIF profile, $z(t)$ is the VDF, and $a(t)$ is the convolution of the transition line shape and any other profile broadening mechanisms such as laser, or instrument broadening and is usually denoted in the literature as the point spread function (PSF) [13].

For analytical functions, solution of Eqn. 2 is trivial. Discrete data with a reasonably high signal to noise ratio (SNR) may employ a number of numerical techniques with mixed results. The introduction of the noise inherent to the measurements will usually create a mathematically ill-posed problem that lacks a unique solution. Noise tends to produce instabilities in the numerical deconvolution process which propagate through the solution and contaminate the results. Deconvolution then becomes a tradeoff between solution smoothness and numerical accuracy. Subsequently, the deconvolution of noisy data may become subjective. Iterative methods attempt to mitigate this issue by incorporating physical constraints in a rigorous methodology with noise analysis to determine the extent of deconvolution possible. However, the effect of noise in real data during deconvolution limits the application of all deconvolution algorithms [13-14].

For discrete data, convolution may be represented by

$$Az = u \quad [3]$$

where u is the convolved vector with noise inherent to the data collection, A is the PSF in matrix format, and z is the desired vector, in this case the VDF. The deconvolution algorithm used in this work is a zeroth order Tikhonov's regularization method [14-15]. Tikhonov's regularization method seeks to solve Eqn. 3 through use of an artificial smoothing function to cure the ill-conditioned nature of the deconvolution. It does this by minimizing an artificial, constrained smoothing function $M^\alpha(z, u)$ defined to be

$$M^\alpha(z, u) = \|Az - u\|^2 - \alpha \|z\|^2 \quad [4]$$

where α is the regularization parameter. The minimization is performed by setting the derivative of $M^\alpha(z, u)$ to zero which yields

$$(A^T A + \alpha I)z = A^T u \quad [5]$$

where I is the identity matrix. Equation 5 may be solved for z . In this work, Eqn. 5 is solved for z using LU decomposition.

The precept of Tikhonov regulation is that a unique, stable solution to the deconvolution may be achieved by minimizing the constrained smoothing function $M^\alpha(z, u)$. Fundamentally, this will generate a stable, single valued solution only so long as the uncertainty of the iterated solution does not exceed the uncertainty (noise) of the original data. Within these constraints, the algorithm is relatively insensitive to noise [15].

The choice of α affects the deconvolution process. Too high of a value will overly smooth the result and too low of a value will allow the noise produce nonphysical results. Happily, regularization provides a mechanism to determine the degree to which deconvolution can proceed [16]. The L-curve is a log-log plot of the norm of the residual versus that of the corresponding norm of the regularized solution. As the regularization parameter is varied, the L-curve provides a convenient graphical tool

for determining the trade off between regularized solution and fit to the data. The vertex of the L-curve denotes the best trade off between these two sources of uncertainty by balancing the magnitude of the solution and the solution smoothness.

The main advantage of the L-curve method is that it allows for a quantitative methodology to determine the optimal regularization parameter α . If an estimate of the noise inherent to the data is available, it is possible to determine similar criterion without generating the multiple deconvolutions required to construct the L-curve. However, experience has shown that noise estimates are not sufficiently accurate and that use of the L-curve in determining the optimum regularization parameter eliminates many of the uncertainties in the noise estimation. Most importantly, the L-curve removes a potential source of experimental bias from the data analysis.

For this effort, the PSF of the LIF data was measured using the apparatus shown in Fig. 2 with several minor modifications. Fluorescence was collected from the low pressure, pass through hollow cathode lamp (<100 Pa) using the 125 mm monochromator with a single 300 mm focal length lens. A typical LIF line profile is shown in Fig. 4 along with a Gaussian curve fit. Although the transition line shape is not strictly symmetrical, a Gaussian profile with a full width at half maximum (FWHM) of 600 MHz fits the data adequately. This PSF accounts for both instrument and line shape effects.

Figure 5 shows a sample axial LIF profile and resulting deconvolved VDF from the Hall thruster channel exit plane where the raw LIF profile is broadest. The data is an average of 5 raw LIF traces of 1000 points filtered with 5 passes of a 25 point second order Savitzky-Golay filter interpolated to 512 points for the deconvolution. The data has an estimated SNR of 50. The PSF is substantially narrower than the broad LIF trace with an equivalent FWHM of 500 m/s. As a result, deconvolution does not substantially change this raw LIF trace. Figure 6 shows a radial distribution located 28 mm downstream from the axial VDF in Fig. 5. Here deconvolution narrows the peak, increasing the peak height by approximately 20% (Note that both raw and deconvolved data are area normalized). The deconvolution of this LIF profile results in a greater change than that seen in Fig. 5 due to the narrower peak in the raw data. Broader features such as that between 2-5 km/s are not affected by the deconvolution. It should also be noted that the deconvolution routine typically produces oscillatory noise near the trace end-points as seen in Fig. 5 and cropped out in Fig. 6.

Deconvolution is not strictly required to estimate xenon ion VDFs from the raw LIF data in this particular plasma discharge. Not performing the deconvolution introduces an uncertainty conservatively estimated to be less than 20%. The majority of the following data will consist of data that has been deconvolved. However, some data with low SNR with broad distributions, especially those near the exit plane, will not be deconvolved to minimize deconvolution induced noise. All such data will be clearly identified.

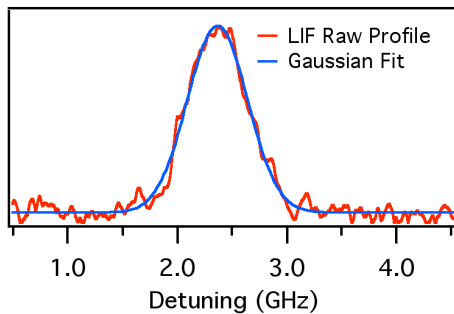


Fig. 4. Hollow cathode discharge lamp LIF profile of xenon ion $5d[4]_{7/2}-6p[3]_{5/2}$ transition and gaussian curve fit used as the PSF.

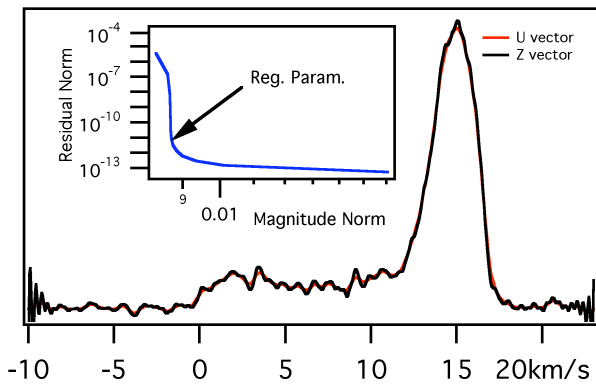


Fig. 5. Exit plane axial LIF profile (U vector), and resulting deconvolved VDF (Z vector). Also shown is the L -curve computed with the location of regularization parameter used. Note the small difference between VDF and LIF profile

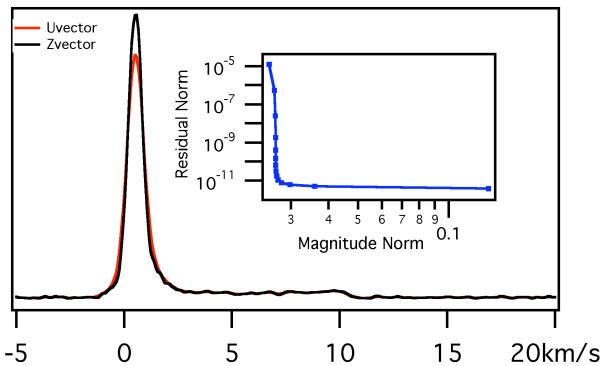


Fig. 6. Radial LIF profile (U vector) 28 mm downstream of exit plane, and resulting deconvolved VDF (Z vector). Also shown is the L -curve computed. Note the sharpening of the peak due to deconvolution is significant due to the relatively narrow distribution relative to the PSF.

Results and Discussion

Understanding and characterizing the near plume region is important in understanding the interaction of the ion plume with the environmental background gas as well as a starting point for the modeling of the plume expansion to determine the affects of thruster placement on thruster/spacecraft interaction. It has been shown previously that the xenon ions emitted from a Hall thruster undergo approximately 50 eV of additional acceleration between the thrusters physical exit plane and cathode plane [17]. The ionic flow evolves in the near plume region and the thruster can not be fully characterized without studying this region in detail. In this specific thruster with its protruding central magnetic pole, the erosion of the boron nitride nose cone is a life limiter. Knowledge of the ionic VDF in this region would aid in the prediction of thruster life and provide guidance constructing longer lived Hall thrusters.

Channel Center VDF Evolution

Figures 7 and 8 show the evolution of the axial and radial VDF with varying distance from the exit plane ($Z = -7$ mm)

through the cathode plane ($Z = +13$ mm) to a distance 28 mm from the exit plane ($Z = +21$ mm). All data in Figs. 7 and 8 is from the center of the acceleration channel ($Y = 12$ mm). In each figure, the VDF data is area normalized and all 8 traces are provided with identical scaling. In both axial and radial data, the VDF retains a fundamental form as the ions travel through the near plume region. However, there are a number of important changes that provide insight of the processes occurring to the ions as they travel through the near plume.

The axial VDF typically consists of a narrow primary peak overlaying a broader distribution of generally low velocity classes. The main peak is accelerated between the exit plane and nose cone tip ($Z = 0$) by approximately 2.1 km/s, from 15,100 to 17,200 m/s. The peak continues to accelerate beyond the nose cone tip, but not as significantly. The central peak also narrows during the external acceleration as each ion gains approximately 47 eV from the exterior electric field. With the corresponding velocity increment dependent on initial velocity, the central peak sharpens. The most interesting portion of the axial VDF evolution along the channel centerline is the appearance of populations of low speed ions. As expected, the broad low energy portion of the ion distribution is depleted during between $Z = -7$ mm and $Z = +1$ as the ions are accelerated. However at $Z = +5$ mm, a new class of low axial velocity ions appears. There continues to be populations of low axial velocity ions appearing beyond $Z > 5$ mm.

The radial VDF data presented in Fig. 8 shows a generally sharp, nearly symmetrical distribution. Similar to the axial data, the radial VDF peaks narrow with increasing distance along the Z axis. This can be explained by the flow divergence, fixed sample volume, and increasing distance from the source. Closer examination of the data reveals that there is a slight asymmetry in the data. A positive velocity tail clearly appears just beyond the nose cone ($Z = 1$ mm). The main radial peak continues to narrow until $Z = 17$ mm, despite the positive velocity tail. By $Z = 21$ mm, this tail feature extends to +10 km/s, approximately 80 eV, and has slightly depressed the VDF peak height.

Figure 9 shows the measured axial VDF at the exit plane as well as a calculated energy distribution and the integrals of each. The axial VDF main peak is located at 15.1 km/s (155 eV) with a width of approximately 4 km/s. The mean axial velocity and kinetic energy are calculated to be 12.4 km/s and 139 eV. Approximately 75% of the flow is in the main peak and it contains approximately 90% of the energy. Interestingly, the small feature at 20.1 km/s has a peak energy of 290 eV which is nearly twice that of the mean and peak energies (139-155 eV). Although the SNR is poor, the values are consistent with charge exchange ions. The radial exit plane VDF data in Fig. 10 show a narrow distribution with a symmetrical distribution within a slightly negative mean velocity -570 m/s (1.3 eV).

Figures 11 and 12 show the corresponding axial/radial VDF data at $Z = +5$ mm. The main axial peak has accelerated to 16.9 km/s (195 eV). The mean axial velocity has increased to 14.0 km/s and the mean kinetic energy is 180 eV. A low velocity axial peak (~2 km/s) first appears at this location accounting for 13% of the flow but less than 2% of the axial energy com-

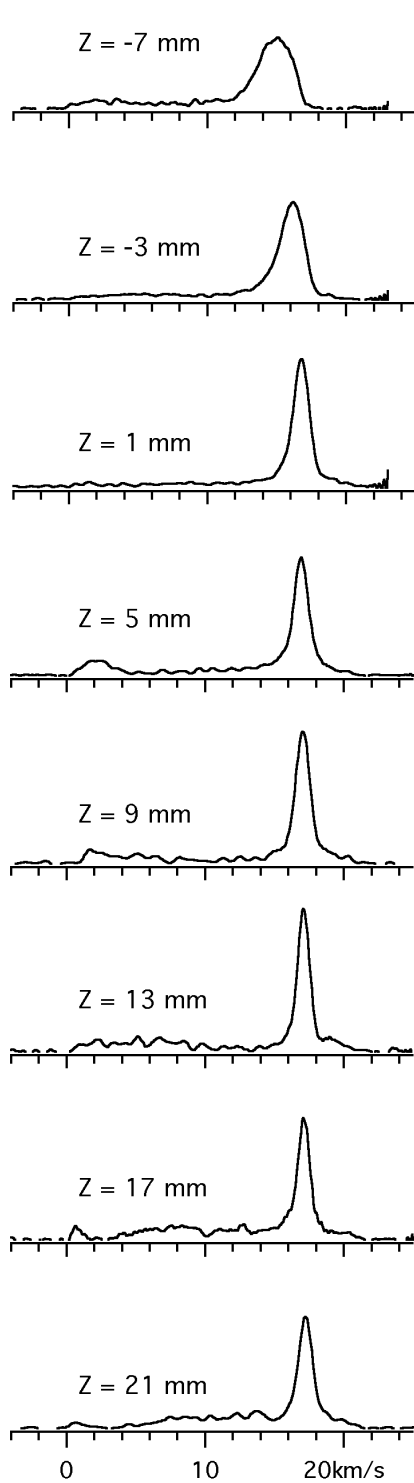


Fig. 7. Axial VDF functions for acceleration channel centerline ($Y = 12$ mm) from the exit plane ($Z = -7$ mm) to 28 mm beyond ($Z = 21$ mm). Note: VDFs are scaled and normalized to unity area.

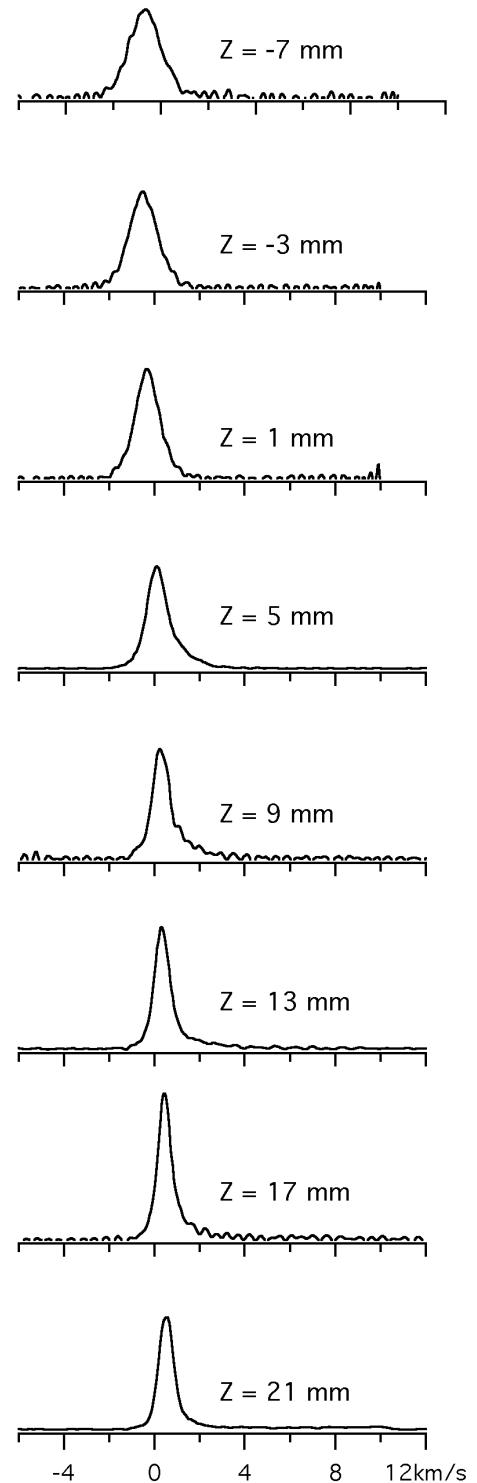


Fig. 8. Radial VDF functions for acceleration channel centerline ($Y = 12$ mm) from the exit plane ($Z = -7$ mm) to 28 mm beyond ($Z = 21$ mm). Note: VDFs are scaled and normalized to unity area.

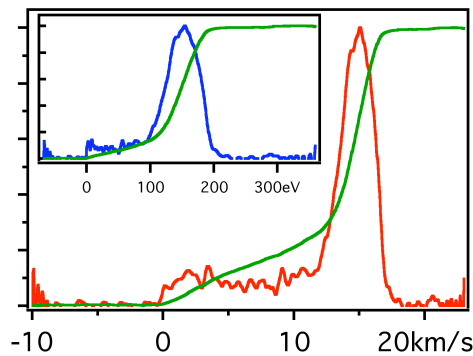


Fig. 9. Centerline axial VDF, inset energy distribution, and relative summations (green) at the thruster exit plane ($Z = -7$ mm). Mean axial velocity and kinetic energy are 12,400 m/s and 139 eV, respectively.

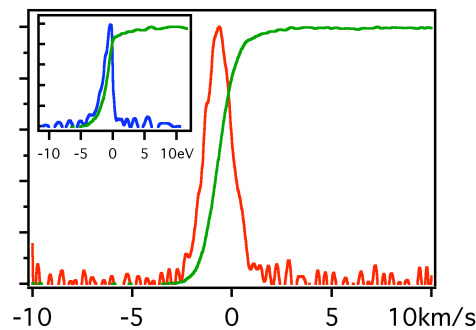


Fig. 10. Centerline radial VDF, inset energy distribution, and relative summations (green) at the thruster exit plane ($Z = -7$ mm). Mean radial velocity and kinetic energy are -570 m/s and -1.3 eV, respectively.

ponent. The main axial peak still contains approximately 75% of the flow and 90% of the energy deposited in the flow. Interestingly enough, the axial VDF shows, a small (~2%) population of ions with velocities greater than 19.17 km/s (250 eV). This is greater than the applied 250 V discharge potential and may be evidence of charge exchange collisions in the plume. The radial distribution in Fig. 12 shows noticeable asymmetry with a positive velocity tail. This is especially evident in the energy distribution which shows 20% of the radial energy to be in this asymmetric feature.

Figures 13 and 14 show the corresponding axial/radial VDF data at $Z = +21$ mm. The main axial peak has accelerated to 17.2 km/s (202 eV). The main axial peak now only contains 65% of the flow and 75% of the flow energy. The mean axial velocity is now 14.8 km/s with a mean axial kinetic energy of 186 eV. Now approximately 6% of the ions have energies greater than 250 eV. This increase can be seen more globally in Fig. 7 as the high velocity tail of the main axial feature grows with Z . The radial VDF in Figure 14 shows a larger fraction of the radial flow (~15%) is now in the high velocity tail which clearly extends to 80 eV and that it now accounts for approximately 65% of the radial energy.

The asymmetry beyond the nose cone is believed to be due to mixing with the flow from the opposite portion of the thruster annulus. The behavior of the radial data is consistent with

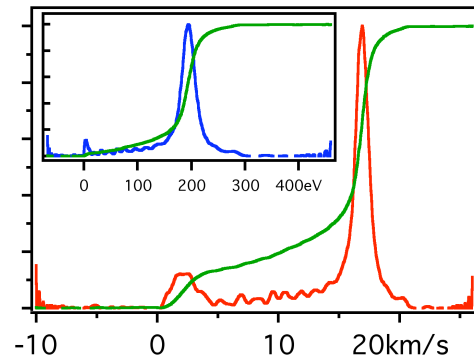


Fig. 11. Centerline axial VDF, inset energy distribution, and relative summations (green) at $Z = 5$ mm. Mean axial velocity and kinetic energy are -13,985 m/s and 180 eV, respectively. Note the appearance of a low velocity ion population.

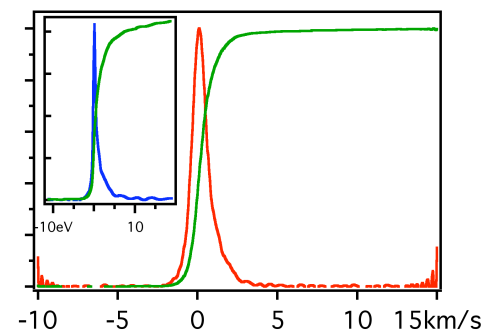


Fig. 12. Centerline radial VDF, inset energy distribution, and relative summations (green) at $Z = 5$ mm. Mean radial velocity and kinetic energy are 400 m/s and 6.5 eV, respectively.

the apparently low and mid range velocity populations in the axial VDF data, especially if collisions between the various populations create low velocity populations. It also appears to be consistent with peak velocity data from further in the plume taken in a previous study which show a distinct second peak appearing further downstream which is clear evidence of cross annular flow [17]. The axial VDF traces in Fig. 7 do show one feature of the axial VDF data which can not be explained by cross annular flow. Beginning just beyond the exit plane, the high velocity tail originating on the main peak becomes noticeable and progressively more prominent with distance from the thruster exit plane. This appears to be evidence of charge exchange collisions between singly and doubly charged xenon ions as previously reported by King in the SPT-100 thruster using parallel plate energy analyzers in the distant plume [18]. The appearance of the very low speed ions beyond $Z = 1$ mm may also be related to charge exchange, but of collisions of singly charged ions with neutrals. However, charge exchange as the primary source low energy ions remains speculative at this time and it is believed that annular cross flow with significant collisionality is the more likely explanation.

VDF Evolution Near Thruster Nose Cone

From the acceleration channel centerline data presented in Figs. 7-14, it is apparent that the ion beam is focused slightly inward. Since Hall thruster lifetime is limited by the erosion of

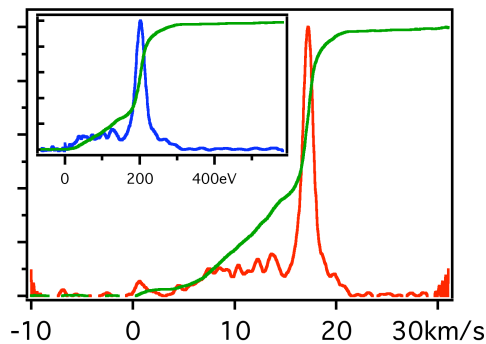


Fig. 13. Centerline axial VDF, inset energy distribution, and relative summations (green) at $Z = 21$ mm. Mean axial velocity and kinetic energy are 14,750 m/s and 186 eV, respectively.

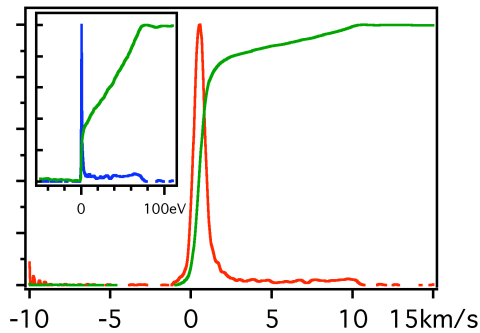


Fig. 14. Centerline radial VDF, inset energy distribution, and relative summations (green) at $Z = 21$ mm. Mean radial velocity and kinetic energy are 1,230 m/s and 19 eV, respectively.

the insulator channel walls and for this thruster also that of the boron nitride nose cone covering the protruding central magnetic pole, it is important to understand interaction of surfaces with the plasma. After an ion strikes a wall, it is typically assumed that full accommodation occurs. The ion recombines with a wall electron to form a neutral and subsequently leaves the wall fully thermalized without a preferential direction. These resultant neutrals may then interact with the plasma in a variety of ways. These include creating regions of higher than expected density with correspondingly higher electron conduction due to increased numbers of collision partners. These recombined ions may also be re-ionized and accelerated by the external electric fields to energies of 40-50 eV (7.5-8.5 km/s). Due to the divergence of Hall thruster's external electric fields, these low energy ions will likely be accelerated with significantly more divergence than the main flow. Understanding this portion of the flow is therefore of great importance to the spacecraft integrator.

Figure 15 shows a survey of the axial and radial ionic VDF data along the protruding central magnetic nose cone of the thruster. This data has not been deconvolved due to the broad LIF profiles and the low SNR. However, all data in Fig. 15 has been area normalized and all graphs contain a common scaling. Figure 15 also shows the relative size and placement of measurement regions as well as the calculated mean axial and radial velocities. These traces are from a single series of LIF traces and contain no averaging, but have been filtered to remove high frequency noise. The flow begins at the exit plane ($Z = -7$ mm)

with an axial VDF with a high proportion of low velocity ions. These are likely a result of the central nose cone geometry that places this measurement region in the lee of the interior portion of the thruster nose cone. The radial VDF at this position shows a divergent flow toward the insulator with a peak at -4 km/s. In Fig. 15, the general trend of the axial VDF data that the higher velocity peak grows as the slow moving ions are externally accelerated. This trend ends at $Y, Z = 6, -4$ mm. Beginning here and extending to the nose cone tip, the axial VDF is increasingly dominated by the low velocity portion of the VDF. The mean axial velocity drops steadily from this point onward and the distributions broaden significantly. At the nose cone tip, the axial VDF is an extremely broad feature with a mean velocity of 1 km/s. It is interesting to note that after some period of running the thruster used in this study, an indentation formed on the nose cone tip. The broad distribution at the nose cone tip ($Y, Z = 0, 0$ mm) in Fig. 15 shows that nearly half the ions in this region are moving toward the thruster and are subsequently sputtering material that would ordinarily be considered to be in the shadow of the nose cone.

The radial distributions in Fig. 15 show a steadily broadening distribution along the nose cone profile. The radial VDF peak velocity also steadily decreases along nose cone; starting at -4 km/s at the exit plane and approaching -8 km/s just prior to the tip. At the nose cone tip, the radial distribution is nearly 20 km/s wide and likely contains ions from both sides of the annulus which contribute to the width of the distribution.

Interestingly at the exit plane ($Z = -7$ mm), there is a weak radial VDF peak at +4 km/s that appears to contain approximately 10% of the apparent population. This may be due to the reflection of the laser off the nose cone producing a spurious signal. This effect has been used before by Cedolin, et al., who used reflection off a Hall thruster anode to eliminate the need for a stationary reference source [19]. However, we can not completely rule out that the signal represents a distinct population of ions. This illustrates one of the difficulties inherent to laser diagnostics for plasma/surface interactions. For the analysis, the possibly spurious signal is retained for calculation of mean velocities since the possibility of ions flowing in away from the nose cone surface can not be completely ruled out, especially further along the nose cone. At the nose cone tip, it appears that there are ions from both sides of the annulus which produce the extremely broad axial and radial distributions. There are some similarities at $Z = -6$ mm where there is also an apparent positive velocity flow. It may be that the small positive velocity portion of the radial VDF is due to leakage around the nose cone of plasma from the opposite portion of the annulus. It is also important to consider the dimensions of the sample volumes which may explain these results.

Exit Plane Profiles

The LIF signal in the linear regime is proportional to both the probed state density and the intensity of the probe beam. Therefore, it is at least theoretically possible to determine relative ionic excited state number densities within the plume. Figure 16 shows the LIF profiles across the exit plane with relative signal intensity information retained. This shows that in the main peak of the distribution, the xenon excited state has twice

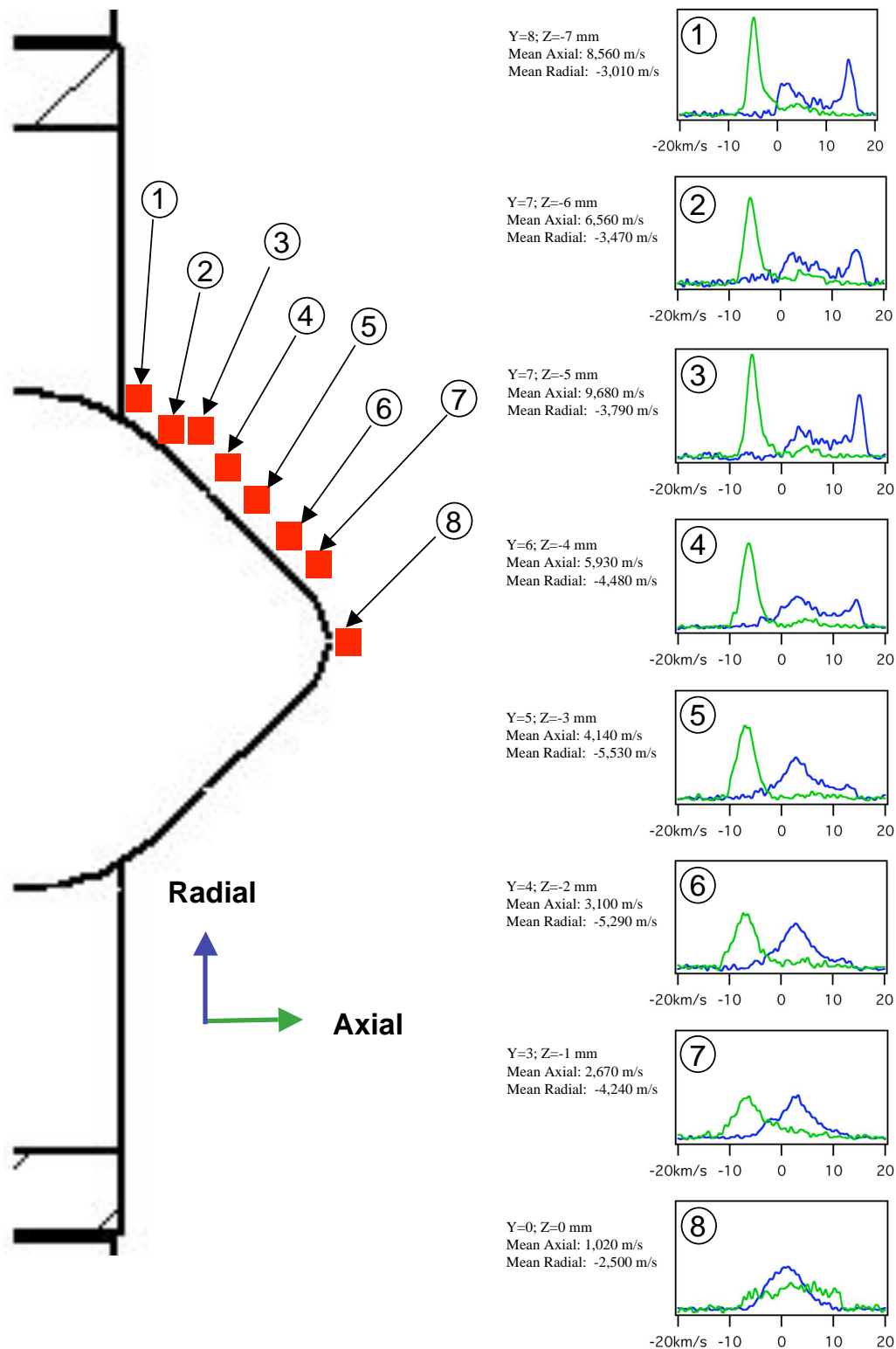


Fig. 15. Axial and radial velocity distributions (not deconvolved) along the nose of the BHT-200-X for the conditions in Table 1. Y and Z coordinates as well as mean velocities are provided for each data set. Note that the VDF data is area normalized and plotted with a common scale.

the number density at the center than at the channel edges. The plasma nearest the inner channel wall ($Y = 8$ mm) exhibits a much larger proportion of low velocity ions than the flow nearest the outer channel wall ($Y = 16$ mm). This pooling of low velocity ions near the inner channel wall may be due to this small thruster's divergent radial magnetic field which results in ions striking the inner walls, recombining, and subsequently ionized to produce the low velocity ions, especially those seen between 0-5 km/s.

However, caution must be taken in the analysis of these data in Fig. 16. It is reasonable to state that the ions may be representative of the local ions at any single location, the method by which this state is populated may vary across the exit plane, and certainly beyond. The population of this state is maintained by the simultaneous processes of radiative decay from/to higher/lower states, and collisional excitation/de-excitation via electron or heavy particle (ion or neutral) collisions. Therefore caution must be taken in this sort of analysis in general, but specifically here where the plasma densities are so variable.

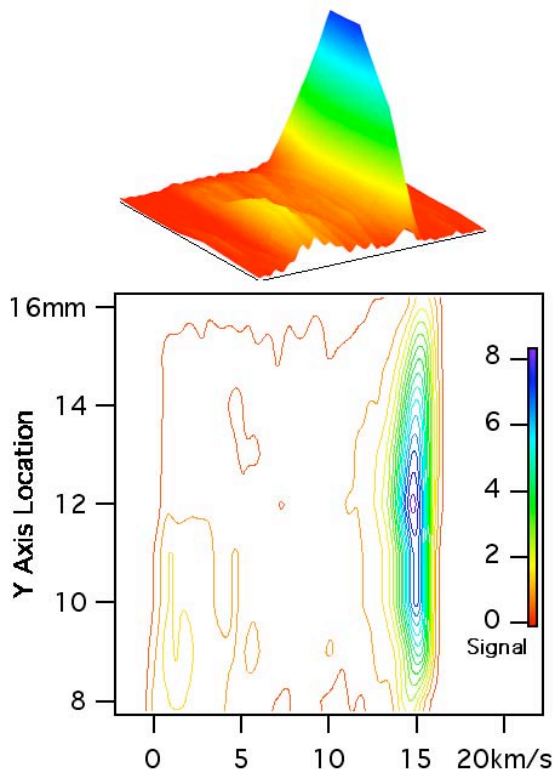


Fig. 16. Exit plane ($Z = -7$ mm) VDF contour and surface plot scaled to LIF signal strength ($5d[4]_{7/2}$ xenon ion excited state). Note the region of high density of low velocity ions along the inner channel ($Y = 8$ mm).

Conclusions

This work has presented a preliminary analysis of the LIF derived velocity distribution functions (VDF) of the $5d[4]_{7/2}$ excited state of xenon in a 200 W BHT-200-X3 laboratory Hall thruster. The ionic VDF evolves considerably within the near

plume region as the ions travel downstream. The axial VDF narrows due to the external addition of approximately 50 eV to the flow. The radial VDF narrows due to the divergence of the flow. Beyond the nose cone, the axial VDF develops a low energy population. In a similar fashion, the radial VDF develops a high velocity tail. Both these effects are most likely due to cross annular flow, momentum exchange collisions, and the resultant mixing of velocity distributions. Charge exchange is being investigated as possible source of the slow moving ions, and there appears to be evidence for charge exchange collisions in the near plume or within the thruster.

The axial VDF appears to evolve differently near the inner insulator wall than at the channel center. The region near the inner wall has a higher proportion of low velocity ions in the VDF and is accelerated 25 eV less than the centerline case. A large fraction of the ions appear to be created near the exit plane at the inner channel insulator wall. The source of the ions is not known, but from the radial VDF data, it is suspected that the slow ions may be the result of ion recombination at the inner wall, followed by local ionization.

Finally, a crude estimate of the relative densities at the exit plane is made. It appears that there are a factor of 4 more fast moving ions in the center of the acceleration channel than at the inner and outer regions. The relative width of the VDF axial main peak is near constant as is the peak velocity. This indicates that these ions are all created in the same potential line within the thruster. The distribution of low velocity ions within the VDF profiles is much stronger in the inner half of the annular acceleration channel, possibly related to the radial magnetic field divergence of this relatively small Hall thruster.

Future Work

These results show that the velocities of the ions accelerated by a Hall thruster can not be well characterized by a single value. We believe that the direct comparison of VDF data will provide the best method to validate numerical methods. We hope to compare these data with those derived from various numerical models. Although bulk velocities have been compared in the past [20], we are only aware of one direct comparison between of VDF data derived from experimental and numerical means [21]. The results of this study show that small changes in model parameters can produce dramatic changes in the predicted plasmas. Although the models appear able to match portions of the flow field, it does not appear possible to predict a Hall thruster ion velocity field a priori. Significant experimental inputs are required.

It would be advantageous to continue this analysis to the interior of the Hall thruster. Many Hall thruster models use experimental current-voltage characteristics to approximate the electron conduction through radial magnetic field. Therefore, it will be possible to refine these models with VDF data. Due to the geometry of the BHT-200-X3 Hall thruster it is possible to cut a slot to provide internal optical access for the acquisition of axial VDF data using the current test apparatus.

It is also important to continue the development of the de-convolution routines into our data reduction methodology. We

hope to develop a first order Tikhonov regularization as well as tune the data collection methods to increase our SNR to produce clearer data for analysis.

Acknowledgments

The author would like to acknowledge the assistance of Garrett Reed in the development of the LIF data acquisition system as well as Lubos Brieda, Justin Koo, and Douglas VanGilder for their discussions of numerical Hall thruster modeling.

References

1. W. A. Hargus, Jr. and M. A. Cappelli, "Laser-Induced Fluorescence Measurements of Velocity within a Hall Discharge," *Applied Physics B*, Vol. 72, pp 961-969, 2001.
2. H. Geisen, T. Krumpelmann, D. Neuschafer, and Ch. Ottinger, "Hyperfine Splitting Measurements on the 6265 Å and 6507 Å Lines of Seven Xe Isotopes by LIF on a Beam of Metastable Xe(3P_{0,3}) Atoms," *Physics Letters A*, Vol. 130, No. 4.5, 11 July, 1988.
3. W. Fischer, H. Huhnermann, G. Kromer, and H.J. Schafer, "Isotope Shifts in the Atomic Spectrum of Xenon and Nuclear Deformation Effects," *Z. Physik*, Vol. 270, No. 113, 1974.
4. L. Bronstrom, A. Kastberg, J. Lidberg, S. Mannervik, "Hyperfine-structure Measurements in Xe II," *Physical Review A*, Vol. 35, No. 1, Jan. 1996.
5. D.H. Manzella, "Stationary Plasma Thruster Ion Velocity Distribution," AIAA-94-3141, *30th Joint Propulsion Conference*, 27-29 June 1994, Indianapolis, IN.
6. J.E. Pollard and E.J. Beiting, "Ion Energy, Ion Velocity, And Thrust Vector Measurements For The SPT-140 Hall Thruster," *3rd International Conference on Spacecraft Propulsion*, 10-13 Oct. 2000, Cannes, France.
7. T.E. Smith, B.B. Ngom, J.A. Linnell, A.D. Gallimore, "Diode Laser-Induced Fluorescence of Xenon Ion Velocity Distributions," AIAA-2005-4406, *41st Joint Propulsion Conference*, 11-13 July, Tucson, AZ.
8. J. E. Hansen and W. Persson, "Revised Analysis of Singly Ionized Xenon, Xe II," *Physica Scripta*, Vol. 36, pp 602-643, 1987.
9. W. Demtroder, *Laser Spectroscopy: Basic Concepts and Instrumentation*, Springer-Verlag, Berlin, 1996
10. W.A. Hargus, Jr. and G. Reed, "The Air Force Clustered Hall Thruster Program," AIAA-2002-3678, *38th Joint Propulsion Conference*, 7-10 July 2002, Indianapolis, Indiana.
11. M.H. Miller and R.A. Roig, "Transition Probabilities of Xe I and Xe II," *Physical Review A*, Vol. 8, pp 480-486, July 1973.
12. C.E. Moore, *Atomic Energy Levels: Volume II*, Washington: National Bureau of Standards, pp 113-123, 1958.
13. P. A. Jansson, *Deconvolution of Images and Spectra*, Academic Press, Inc., San Diego, 1997.
14. W.H. Press, S.A. Teukolsky, W.T. Vetterling, and B.P. Flannery, *Numerical Recipes in Fortran: The Art of Scientific Computing*, Cambridge University Press, Cambridge, 1992.
15. G.M. Petrov, "A Simple Algorithm for Spectral Line Deconvolution," *Journal of Quantitative Spectroscopy and Radiative Transfer*, Vol. 72, pp 281-287, 2002.
16. P.C. Hansen, "Analysis of Discrete Ill-Posed Problems by Means of the L-Curve," *SIAM Review*, Vol. 34, pp 561-580, 1992.
17. W.A. Hargus, Jr. and C.S. Charles, "Near Exit Plane Velocity Field of a 200 W Hall Thruster," AIAA-2003-5154, *39th Joint Propulsion Conference*, 20-23 July 2003, Huntsville, AL.
18. L.B. King, *Transport-Property and Mass Spectral Measurements in a Hall-Effect Space Propulsion Thruster*, Ph.D. Dissertation, Aerospace Engineering, University of Michigan, May 1998.
19. R.J. Cedolin, *Laser-Induced Fluorescence Diagnostics for Xenon Plasmas*, Ph.D. Dissertation, Mechanical Engineering, Stanford University, June 1997.
20. I.D. Boyd and J.T. Yim, "Modeling of the Near Field Plume of a Hall Thruster," *Journal of Applied Physics*, 1 May 2004, Vol. 95, No. 9, pp 4575-4584.